JVI Journals.ASM.org

Capsid Antibodies to Different Adeno-Associated Virus Serotypes Bind Common Regions

Brittney L. Gurda,[a]* Michael A. DiMattia,[a]* Edward B. Miller,[a]* Antonette Bennett,[a] Robert McKenna,[a] Wendy S. Weichert,[b] Christian D. Nelson,[b]* Wei-jun Chen,[c] Nicholas Muzyczka,[c] Norman H. Olson,[d] Robert S. Sinkovits,[d]* John A. Chiorini,[e] Sergei Zolotutkhin,[f] Olga G. Kozyreva,[g] R. Jude Samulski,[g] Timothy S. Baker,[d] Colin R. Parrish,[b] Mavis Agbandje-McKenna[a]

Deptartment of Biochemistry and Molecular Biology, University of Florida, Gainesville, Florida, USA[a]; Baker Institute for Animal Health, Department of Microbiology and Immunology, College of Veterinary Medicine, Cornell University, Ithaca, New York, USA[b]; Department of Molecular Genetics and Microbiology, University of Florida, Gainesville, Florida, USA[c]; Department of Chemistry and Biochemistry, and Division of Biological Sciences, University of California—San Diego, San Diego, California, USA[d]; Molecular Physiology and Therapeutics Branch, National Institute of Dental and Craniofacial Research, National Institutes of Health, Bethesda, Maryland, USA[e]; Division of Cellular and Molecular Therapy, Department of Pediatrics, University of Florida, Gainesville, Florida, USA[f]; Department of Pharmacology, Gene Therapy Center, University of North Carolina at Chapel Hill, Chapel Hill, North Carolina, USA[g]

Interactions between viruses and the host antibody immune response are critical in the development and control of disease, and antibodies are also known to interfere with the efficacy of viral vector-based gene delivery. The adeno-associated viruses (AAVs) being developed as vectors for corrective human gene delivery have shown promise in clinical trials, but preexisting antibodies are detrimental to successful outcomes. However, the antigenic epitopes on AAV capsids remain poorly characterized. Cryo-electron microscopy and three-dimensional image reconstruction were used to define the locations of epitopes to which monoclonal fragment antibodies (Fabs) against AAV1, AAV2, AAV5, and AAV6 bind. Pseudoatomic modeling showed that, in each serotype, Fabs bound to a limited number of sites near the protrusions surrounding the 3-fold axes of the T=1 icosahedral capsids. For the closely related AAV1 and AAV6, a common Fab exhibited substoichiometric binding, with one Fab bound, on average, between two of the three protrusions as a consequence of steric crowding. The other AAV Fabs saturated the capsid and bound to the walls of all 60 protrusions, with the footprint for the AAV5 antibody extending toward the 5-fold axis. The angle of incidence for each bound Fab on the AAVs varied and resulted in significant differences in how much of each viral capsid surface was occluded beyond the Fab footprints. The AAV-antibody interactions showed a common set of footprints that overlapped some known receptor-binding sites and transduction determinants, thus suggesting potential mechanisms for virus neutralization by the antibodies.

Antibodies that are elicited against virus capsids represent a critical component of the host protective response in vertebrates. For most viruses, they control both the susceptibility of an animal to infection and also the recovery from disease. For human gene delivery, the presence of preexisting antibodies or antibodies that develop after administration of viral vectors can create significant complications for the application or reapplication of therapies (1–4). The host antibody responses initiate through the binding and activation of B cells and are originally composed of low-affinity IgM variants; the B cells are subsequently selected for enrichment of higher-affinity antibody variants, which class-switch to form IgG1 and other subtypes. However, details of the production of effective immune responses against viral antigens and the structural features of epitopes on viruses are still only partially understood (5–8).

Adeno-associated viruses (AAVs) consist of a T=1 icosahedral capsid composed of three related, overlapping viral structural proteins (VP1, VP2, and VP3), which differ in their N termini, while the unique N-terminal region of VP1 (VP1u) is essential for capsid trafficking within the cell during infection (9–12). VP3 is contained entirely within the sequence of VP2, which is, in turn, contained within VP1. In the three-dimensional (3D) structures of AAVs determined thus far, only the ~520 amino acids (aa) within the VP3 common region have been observed (13–17). VP3 contains an eight-stranded β-barrel core, with the β-strands linked by extended loops that form the capsid surface (Fig. 1A). These loops, the largest of which is the GH loop (~230 aa) located between the βG and βH strands, also contain stretches of β-strand structure (Fig. 1B). The loops exhibit the highest sequence and structural variation in the VP3 region and contain nine structurally variable regions (VRs; VR-I to VR-IX) (defined in reference 14) (Fig. 1A and B), which have roles in receptor attachment, tissue transduction, and antigenicity (reviewed in references 14, 17, 18, 19, and 20). The AAV capsid surface topology (Fig. 1A) is characterized by prominent features, such as depressions at the icosahedral 2-fold axis and around a channel-like structure at the 5-fold axis and protrusions that surround each icosahedral 3-fold

Received 4 March 2013 Accepted 3 June 2013

Published ahead of print 12 June 2013

Address correspondence to Mavis Agbandje-McKenna mckenna@ufl.edu.

* Present address: Brittney L. Gurda, Gene Therapy Program, Department of Pathology and Laboratory Medicine, University of Pennsylvania, Philadelphia, Pennsylvania, USA; Michael A. DiMattia, National Institutes of Health, National Institute of Arthritis and Musculoskeletal and Skin Diseases, Laboratory of Structural Biology Research, Bethesda, Maryland, USA; Edward B. Miller, Department of Chemistry, Columbia University, New York, New York, USA; Christian D. Nelson, Department of Molecular Biology, Cell Biology and Biochemistry, Brown University, Providence, Rhode Island, USA; Robert S. Sinkovits, San Diego Supercomputer Center, University of California—San Diego, La Jolla, California, USA.

Copyright © 2013, American Society for Microbiology. All Rights Reserved.

doi:10.1128/JVI.00622-13

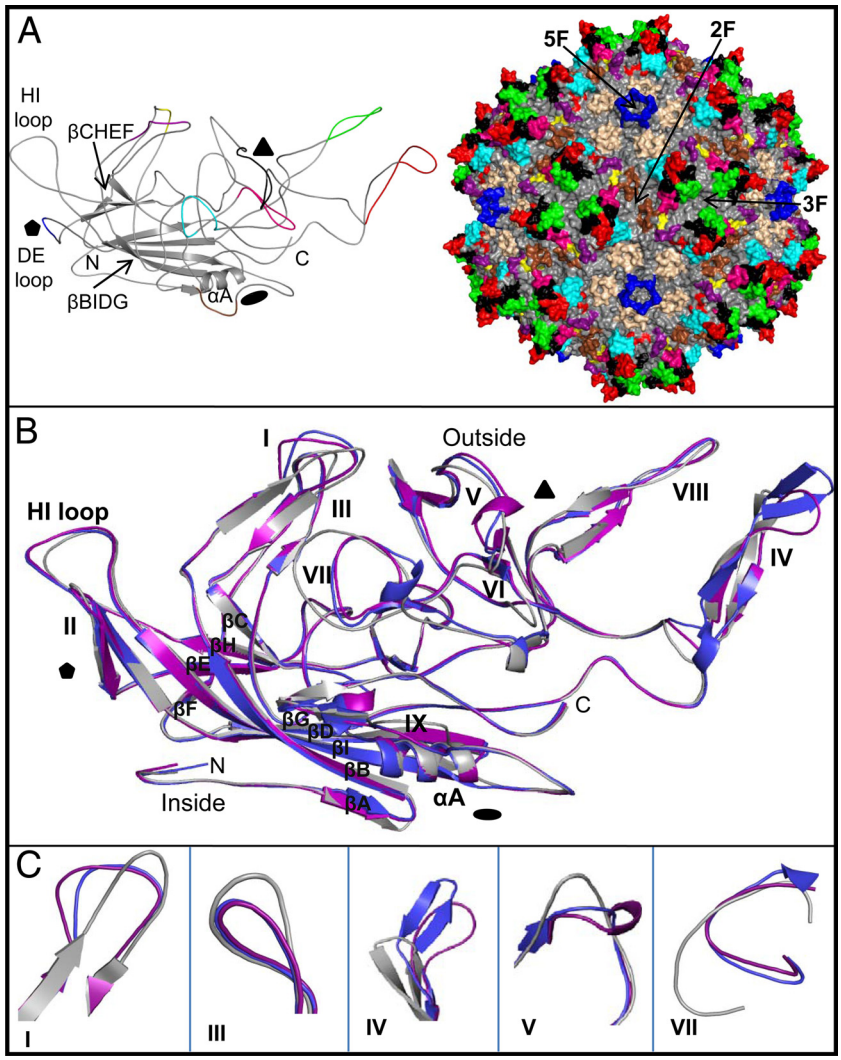

FIG 1 Variable regions on the AAV capsid surface. (A) Ribbon diagram (left) of an AAV2 VP3 monomer highlights the eight β-strands that make up the core β-barrel (gray ribbon) and loops inserted between the strands that make up the capsid surface. The nine AAV variable regions (VR-I to -IX) (defined in reference 14) are colored as follows: I, purple; II, blue; III, yellow; IV, red; V, black; VI, hot pink; VII, cyan; VIII, green; and IX, chocolate. The two β-sheets of the β-barrel are indicated by arrows, and the αA helix, the DE (between βD and βE) and HI (between βH and βI) loops, and N and C termini are labeled. The approximate positions of the 2-, 3-, and 5-fold axes are indicated by filled oval, triangle, and pentagon symbols, respectively. At right is an AAV2 capsid (gray; assembled from 60 VP3 monomers) showing the location of the VRs, colored as described for panel A, with the HI loop shown in wheat. The approximate positions of the 2-fold (2F), 3-fold (3F), and 5-fold (5F) axes are indicated by arrows. (B) Superposition of the VP3 monomers for AAV1 (purple), AAV2 (blue), and AAV5 (gray) showing the variable regions (VR-I to -IX), β-sheets, αA helix, and the HI loop. The regions with the most notable differences in structure between these viruses, VR-I, -III, -IV, -V, and -VII, are highlighted (C). AAV6 is structurally identical to AAV1 and is not shown. Inside/outside labels indicate the VP regions at the interior/exterior capsid surface.

axis. The depressions vary in width, while the protrusions vary in width and height among different AAVs (14, 15).

Many naturally occurring AAV serotypes and genetic variants have been identified from humans and nonhuman primates, and others have been isolated from numerous vertebrates, including species from the families *Equidae*, *Bovidae*, *Phasianidae*, and *Viperidae* (21–34). Among the viruses isolated from human and nonhuman primate tissue, several have been defined as serotypes because they exhibit little or no antigenic cross-reactivity with sera specific for other characterized serotypes (AAV1 to AAV5 and AAV7 to AAV9, with AAV6 being very similar to AAV1) (27, 35). To date, the genetic variants AAV10 and AAV11 (28), AAV12 (29), and AAV VR-942 (36) have not been serologically characterized. In addition to exhibiting antigenic differences, these serotypes also differ in tissue tropism and receptor binding specificity and affinity. Each AAV serotype has a distinct ability to transduce cells and tissues of different hosts when the same transgene is packaged, indicating that the capsid itself dictates these differences (27, 37). Many human clinical trials have employed AAV2, the most studied serotype, but other serotypes and engineered variants are now being developed in a quest to generate vectors with improved tissue specificity and transduction efficiency, while also avoiding the effects of preexisting neutralizing antibodies (see, e.g., reference 38).

Most people have detectable antibodies against one or more of the AAV serotypes, with AAV2 being the most prevalent, followed

by AAV1 (39). A small study of 129 people suffering from cystic fibrosis and 37 unaffected individuals showed that 20 to 30% were seropositive for AAV6 and that 10 to 20% were seropositive for AAV5 (40). Low levels of preexisting antibodies were also found against AAV7 and AAV8, which were originally isolated from nonhuman primates, whereas little or no human antibody reactivity was detected against rhesus macaque variant AAVrh32.33 (39). Low levels of anti-AAV capsid antibodies can significantly reduce the effectiveness of gene therapy trials and may also induce more robust inflammatory responses due to the formation of capsid-antibody immune complexes (4, 41–44). For example, examination of AAV-specific memory T and B cells in mice showed that the reduction in virus transduction was primarily caused by AAV-binding antibodies, which were partially cross-reactive and did not specifically require AAV-neutralizing antibodies, $CD8^+$ T cells, natural killer (NK) cells, or natural killer T (NKT) cells (45). The route of delivery of the vector can also affect the breadth of the antibody responses (46). Approaches taken to avoid the effects of antibodies include suppression of the immune response with cyclosporine and other drugs, activation of regulatory $CD4^+$ T cells, and use of alternative virus serotypes as vectors (47–49). Unfortunately, each of these approaches has its disadvantages, a fact which introduces variability that can complicate already challenging therapeutic approaches.

Little is known about the antigenic structures of AAV capsids and how they interact with the antibodies that have been generated against them. A small number of mouse monoclonal antibodies (MAbs) have been examined that recognize AAV2 capsids (50) and have been raised against other serotypes (10, 51, 52). Mutational analysis, peptide insertions and deletions, and linear epitope mapping methods have been used to characterize the binding of MAbs to AAV2 (50, 53). Most of these MAbs recognize conformational epitopes involving capsid structures comprised of two or more surface loops, with the recognition disrupted when capsids are disassembled and/or denatured. Recently, the binding site for a neutralizing antibody against AAV8, ADK8, was characterized by cryo-electron microscopy (cryo-EM) and 3D image reconstruction (cryo-reconstruction) combined with biochemical and molecular approaches (54). This antibody binds to the protrusions that surround the icosahedral 3-fold axes and affects a trafficking step post-cell attachment and pre-nuclear entry (54). A similar structure determination strategy recently confirmed the binding site of A20, a conformational mouse monoclonal used extensively in the field, on its target antigen AAV2 (55). This neutralizing MAb bound at a different site on the wall between the 2- and 5-fold axes (plateau) and the floor of the depression surrounding the 5-fold channel (canyon). The neutralizing mechanism for A20 is unknown, but like ADK8 against AAV8, it also appears to occur at a postentry step.

Here, cryo-reconstruction methods were used to determine the structures of four different AAV-Fab (fragment antibody) complexes bound to three different AAV serotypes, AAV1, AAV2, and AAV5, with one of the AAV1 Fabs also complexed to the closely related AAV6 capsid. All Fabs bound either on the top or the side of a 3-fold protrusion, except for AAV5, where the binding footprint extended from the protrusion toward the 5-fold channel. The proposed footprints for the Fabs on the different AAVs mostly overlapped one another and covered receptor binding sites, such as the heparan sulfate proteoglycan (HSPG) site on the AAV2 and AAV6 capsids (56–58) and a proposed sialic acid binding site in AAV5 (59). These results and recently published cell binding data (52) suggest that virus neutralization by the antibodies investigated occurs via a steric hindrance mechanism, with the exception of the case of AAV5, which was not neutralized.

MATERIALS AND METHODS

Production and purification of recombinant AAV VLPs. Virus-like particles (VLPs) of AAV serotypes AAV1, AAV2, AAV5, and AAV6 were expressed from recombinant baculoviruses that encoded the AAV capsid open reading frame (ORF). These constructs were produced using a Bac-to-Bac system (Gibco BRL) as previously described for AAV1, AAV5, and AAV6 (16, 60, 61). Baculovirus stocks were grown in Sf9 insect cells at 28°C using Sf-900 II SFM medium (Gibco/Invitrogen Corporation). VLPs were released from the cells by three rapid freeze-thaw cycles in lysis buffer (50 mM Tris-HCl, pH 8.0, 100 mM NaCl, 1 mM EDTA, 0.2% Triton X-100), with the addition of Benzonase (Novagen) in the final cycle. The resulting sample was centrifuged at 10,000 × *g* for 15 min at 4°C to remove cellular debris. For AAV1, AAV5, and AAV6, the supernatant was diluted with TNET buffer (50 mM Tris-HCl, pH 8.0, 100 mM NaCl, 1 mM EDTA, 0.2% Triton X-100) and pelleted through a 20% sucrose cushion at 45,000 × *g* for 3 h at 4°C. The pellet was resuspended overnight at 4°C and then banded on a step gradient (5 to 40% sucrose) at 35,000 × *g* for 3 h at 4°C. VLPs were extracted from the 25% fraction and dialyzed overnight against phosphate-buffered saline (PBS) with gentle stirring at 4°C. AAV2 VLPs were purified on discontinuous step gradients of iodixanol (5,5′-[(2-hydroxy-1,3 propanediyl)bis(acetylamino)]bis[*N*,*N*′-bis(2,3dihydroxypropyl-2,4,6-triiodo-1,3-benzenecarboxamide]) (OptiPrep; Nycomed), prepared by following previously described protocols (62). After centrifugation at 69,000 × *g* for 1 h at 18°C, the 25 to 40% step interface was collected with a needle and syringe, diluted 2-fold with a low-salt buffer (20 mM Tris-HCl, pH 8.5, 15 mM NaCl), and loaded onto a heparin-agarose (H6508; Sigma) column with a 2.5-ml bed volume equilibrated with PBS-MK buffer (1× PBS containing 1 mM $MgCl_2$ and 2.5 mM KCl). The column was washed with PBS-MK buffer, and the sample was eluted with PBS-MK–1 M NaCl. The eluted fraction was dialyzed against PBS as described above for the other AAV serotypes. Approximate concentrations for all of the AAV VLPs were calculated using optical density readings at a wavelength of 280 nm and an extinction coefficient of 1.7 for concentration in mg/ml. The VLP concentrations were adjusted to ~5 to 10 mg/ml using Centricon filters (100,000-molecular-weight cutoff; Amicon), and the purity and integrity of each VLP sample were monitored using SDS-PAGE and negative-stain electron microscopy (EM), respectively.

Production and purification of monoclonal antibodies and fragments. The C37-B MAb against AAV2 was produced as previously reported (50). Monoclonal antibodies against AAV1 and AAV5 (Table 1) were prepared as described by Harbison et al. (52). Hybridomas were cultured in Dulbecco's minimal essential medium with 10% fetal bovine serum and grown in gas-permeable culture bags in 500-ml volumes. Intact IgGs (for AAV1, AAV2, and AAV5) were purified using Hi-Trap Protein G HP columns (GE Healthcare) and eluted from the column with glycine HCl, at pH 3.0, into collection tubes containing 200 μl of 1 M Tris-HCl, pH 9.0, to ensure a final pH of 7.5 to 8.0. Purified IgGs were dialyzed overnight into 20 mM sodium phosphate (pH 7.0)–10 mM EDTA and then concentrated to ~20 mg/ml. Samples were then incubated with activated immobilized papain (Pierce) at an enzyme/substrate ratio of 1:160 (wt/wt) at 37°C for ~12 h. The cleaved sample was loaded on a Hi-Trap Protein A column (GE Healthcare) to remove the Fc regions, and the Fabs were further purified using gel filtration on a Superdex 75 10/60 column (GE Healthcare).

Sequencing of IgG complementarity-determining regions (CDRs). The sequences of the heavy- and light-chain variable domains of the AA5H7.D11 (5H7), AA4E4.G7 (4E4), and BB3C5.3C5 (3C5) IgGs were determined by reverse transcriptase PCR using various combinations of mouse IgG-specific primers. Products were cloned into plasmids and se-

TABLE 1 Cryo-EM data collection and model fitting statistics

AAV:Fab complex	No. of micrographs[a]	Defocus setting (μm)[b]	No. of particle images boxed[c]	Resolution (Å)[d]	CC value(s)[e]
AAV1:4E4	95	1.5–3.0	2,376 (1,914)	12	0.89,* 0.77‡
AAV1:5H7	31	1.25–3.0	313 (262)	23	0.89,† 0.69‡
AAV2:C37-B	149	1.5–3.0	4,731 (4,392)	11	0.82‡
AAV5:3C5	122	1.25–3.0	2,806 (2,552)	16	0.87‡
AAV6:5H7	49	1.0–3.0	5,265 (2,527)	15	0.89,† 0.69‡

[a] Recorded with a CCD camera (4,000 by 4,000 pixels).
[b] Range of objective lens defocus settings.
[c] Values in parentheses are the number of particles used in reconstruction.
[d] Estimate of resolution limit, rounded to nearest Å unit, based on a Fourier shell correlation threshold of 0.5 (72).
[e] Correlation coefficient values for all atom models for Fab and capsid, which reflect the agreement between the model and experimental density maps at the specified resolution. Values were calculated during the map-in-map fitting program provided in Chimera (73). *, calculated with an occupancy of 0.5; †, calculated with an occupancy of 0.3; ‡, calculated with an occupancy of 1.

quenced, and the DNA and protein sequences were determined. The C37-B IgG (50) was not sequenced.

Antibody model building. The IgG variable region sequences for 5H7, 4E4, and 3C5 were submitted to the Web Antibody Modeling (WAM) server (http://antibody.bath.ac.uk/index.html) to generate 3D models of their CDRs. This server generates the model piece by piece for the heavy and light chains and the canonical loops based on the WAM algorithm (http://antibody.bath.ac.uk/algorithm.html). Briefly, homology modeling was used to build the heavy- and light-chain framework of each antibody structure. The canonical loops were also built through homology modeling with five rounds of minimization to smooth out joint regions. The more diverse, noncanonical regions were built using the combined antibody modeling algorithm (CAMAL) (63).

Preparation of Fab:VLP complexes. VLPs (~5.0 to 10.0 mg ml^{-1}) were mixed with Fabs at a ratio of approximately two Fab molecules per potential binding site on the capsid (molar ratio of ~120:1 for Fab:VLP). Complexes were incubated at 4°C for 1 h and then checked by negative-stain EM for visual confirmation of successful VLP decoration by Fabs prior to sample freezing and cryo-EM imaging.

Cryo-EM data collection. Small aliquots (3.5 μl) of AAV:Fab complexes were vitrified using standard rapid freeze-plunging procedures (64, 65). Briefly, this involved applying specimen samples to Quantifoil holey film grids (Quantifoil Micro Tools GmbH, Germany) or homemade grids with continuous carbon films that had been glow discharged for ~15 s in an Emitech K350 glow-discharge unit, blotting the grids for ~5 s with filter paper, plunging the grids into liquid ethane at −193°C with a manual freezing device, and transferring the frozen grids to liquid nitrogen and then into an FEI Tecnai Polara sample holder. The samples were maintained in a vitrified state and imaged in an FEI Tecnai G^2 Polara electron microscope operated at 200 keV, at a nominal magnification of ×59,000 and under low-dose conditions (~25 electrons/$Å^2$) and with the objective lens underfocused by 1.25 to 3.0 μm. Images were recorded with a Gatan Ultrascan 4000 charge-coupled-device (CCD) camera at a nominal step size of 1.883 Å/pixel, saved in Gatan DM3 format, and later converted to a tiff format for processing.

Three-dimensional image reconstructions of AAV:Fab complexes. Individual particle images were extracted from the micrographs and preprocessed, and their defocus values were estimated using the RobEM program (http://cryoEM.ucsd.edu/programs.shtm) (66). The AUTO3DEM program (67) was used as previously described (68) to generate an initial, low-resolution (~30 Å) 3D reconstruction of each complex from a set of 150 particle images using the random-model computation procedure (69). This reconstruction was used to initiate full orientation and origin determination as well as refinement of the entire set of images for each complex using the latest version of AUTO3DEM (67). Corrections to compensate for the effects of phase reversals caused by the microscope contrast-transfer function were performed as previously described (70, 71), but amplitude corrections were not applied. Final 3D maps, reconstructed from the selected particle images, were estimated to be reliable to between 11- and 23-Å resolution (Table 1), based on a conservative Fourier shell correlation threshold of 0.5 (72). The absolute handedness of each reconstructed density map was adjusted if necessary based on knowledge of several AAV crystal structures (13, 16; also unpublished data) (Research Collaboratory for Structural Bioinformatics [RCSB] Protein Data Bank [PDB] numbers 3NG9 and 3NTT for AAV1 and AAV5, respectively). Graphical representations of the reconstructed maps were generated with the RobEM (http://cryoEM.ucsd.edu/programs.shtml) and Chimera (http://www.cgl.ucsf.edu/CHIMERA) visualization software packages (66, 73).

Fitting of atomic and pseudoatomic models into cryo-EM density maps. The coordinates of the 60-mer all-atom VP3 molecules (for each capsid) taken from the crystal structures of AAV1 (PDB accession number 3NG9), AAV2 (PDB accession number 1LP3) (13), AAV5 (PDB accession number 3NTT), and AAV6 (PDB accession number 30AH) (16) were extracted and docked as rigid bodies into the corresponding density maps of the AAV:Fab complexes using the COLORES program in the SITUS software package, version 2.3 (74). Following visual inspection of the docked models in the program COOT (75), the absolute scale of each map was determined by generating a series of AAV:Fab cryo-reconstructions at various sizes using the program Uniconv (http://cryoEM.ucsd.edu/programs.shtm) and comparing these to an electron density map that was computed from structure factors calculated for each docked homology model ("model map") at cell dimensions and grid sizes matching each of the scaled maps. The respective cryo-reconstructions and model maps were then normalized by means of the program MAPMAN (http://xray.bmc.uu.se/usf/mapman_man.html) (76) and compared using the program's similarity function. The highest correlation coefficients for the maps were obtained for pixel sizes ranging from 1.800 to 1.883 Å (the original scale), and these values were then used to compute each AAV:Fab density map at the correct size.

Difference maps were generated in MAPMAN using the operation function (OP), which subtracted a model map from the corresponding, scaled AAV:Fab cryo-EM density map. Positive difference density, representing portions of structure not accounted for by the capsid atomic model, was interpreted as the bound Fab. Initial pseudoatomic modeling of the Fab densities used the coordinates of three generic Fab structures (PDB 2FBJ (IgA) (77), 8FAB (IgG1) (78), and 1ETZ (IgG2B) (79) to assess different elbow angles and variable region structures and, in particular, the complementarity-determining region 3 (CDR3). For AAV2:C37B (for which there was no WAM model), density corresponding to a single Fab was extracted from the reconstruction using the voledit program in SITUS (74), and the 2FBJ Fab coordinates were manually fit within the density, followed by refinement with the "fit-in-map" function in Chimera (80). The fit with the highest correlation coefficient was accepted as the final fit. The PDBs for the 8FAB and 1ETZ Fabs were then aligned with the docked 2FBJ Fab to assess the effects of the elbow angles and CDR structures on the overall fit and analysis. The 5H7 and 4E4 Fabs against AAV1 had overlap between the footprints of their bound Fabs and were thus docked differently. The 2FBJ Fab coordinates were manually docked into the positive density for one Fab in each difference map using Chimera (74), and a "full" capsid pseudoatomic model of each AAV:Fab complex was generated by applying icosahedral (5-3-2 point group) symmetry to the VP3:Fab heterodimer model. Structure factors were calculated from the VLP:Fab pseudoatomic model coordinates using the bsf function in the Bsoft program (81), taking partial occupancy into account where relevant, and electron density maps were generated. The fit-in-map function in Chimera was used to compare each AAV:Fab cryo-reconstruction to the corresponding map of the AAV:Fab model for quantitative assessment of the Fab docking. The WAM models for the sequenced CDRs of 5H7 and 4E4 were then superimposed onto the corresponding docked portion of the

TABLE 2 Epitopes proposed for the AAV:Fab complexes and their footprint areas

AAV:Fab complex	Proposed epitope		Surface area (Å^2)[c]
	Name	Description[a]	
AAV1:4E4	VR-IV	456-AQNK-459	1,197
	VR-V	492-TKTDNNN-498 (3-fold)[b]	
AAV1(AAV6):5H7[d]	VR-V	T494 + 496-NNNS-499	1,360
	VR-VIII	582-VN-583 + 588-STDPATGD-595 + H597	
AAV2:C37-B	VR-V	492-SADNNNS-498	1,230
	VR-VIII	585-RGNRQ-589 (3-fold)[b]	
AAV5:3C5			
Site A	VR-I	254-SVDGSNAN-261	1,728
	VR-III	374-DN-375	
	VR-V	R483, 485-SVSAFATT-492, R494, E496, 499-GAS-501	
Site B	VR-I	Q246	1,137
	VR-VII	N530, 532-QPANPGT-538	
	HI loop	S651, 653-VP-654, 656-SS-657 (5-fold)[b]	
	VR-IX	704-DSTGE-708	

[a] Residue numbering corresponds to that for each of the individual serotypes.
[b] Symmetry relation of residues to the reference VP monomer.
[c] Surface area calculation taken from PDBePISA (84) and rounded to the nearest Å^2.
[d] AAV1(AAV6), 5H7 cross-reacts with AAVI and AAV6. Capsid residues 582-VN-583 and H597 near VR-VIII and T494 near VR-V flank (+) the indicated sites but do not interact directly with the CDRs in the docked Fab models.

2FBJ structure with the secondary structure matching (SSM) superimpose operation in COOT (82). This enabled the identification of the regions of each AAV capsid surface that interacts with the Fab loop regions. All visualization and analysis of these models were performed with Chimera (73) and PyMOL (version 1.3r1; Shrodinger, LLC, New York, NY). A similar strategy was used for fitting 5H7 bound to AAV6. Fitting for the 3C5 Fab (bound to AAV5) density involved using a similar IgG isotype, IgG3 (PDB 3IJH) (83), and manually docking the four regions (heavy and light chains and variable and constant regions) into the Fab density. The correlation coefficient between the reconstructed density and fitted complex model was calculated as described above for the AAV1:Fab complexes. Two sites were chosen as the potential Fab contact sites based on proximity of high sigma threshold density to the capsid surface. All docked Fabs and AAV monomers were analyzed with the programs COOT (75) and PDBePISA (84) to further assess the interfaces in the proposed epitopes. Interacting VP and Fab residues were defined as being within 4.0 Å in PDBePISA (84).

RESULTS

The structures of five different AAV VLP:Fab complexes were examined by means of cryo-reconstruction methods at estimated resolution limits ranging from 11 to 23 Å (Tables 1 and 2; Fig. 2). The 5H7 Fab was complexed with AAV1 and AAV6 since it cross-reacts with both viruses. With the exception of the 3C5 antibody against AAV5, all other antibodies used in this study have been shown to be neutralizing (50, 52). For each complex, the final reconstructed density map was initially scaled to the coordinates of the corresponding AAV capsid crystal structure to determine an absolute map scale (pixel size) prior to the calculation of difference density maps for interpretation and pseudoatomic model building for the bound Fabs (see Materials and Methods). This conservative protocol avoids potential pitfalls of overfitting and does not alter the target map or the input coordinates to allow for conformational differences between the two components. The correlation coefficients computed when cryo-reconstructed and model maps were compared, based on site occupancy, ranged from 0.82 to 0.89 (Table 1). These values support the validity of the models generated for the complexes: variation likely arises from the use of generic Fab structures and sequences and because actual elbow angles are not known. The binding sites (footprints or epitopes) for the four different Fabs on the five AAV capsid surfaces were analyzed to define the contact between AAV VP3 residues and the CDRs of the Fab models. The surface areas occluded by the Fabs on the AAV capsids (Table 2) were within the range previously reported for antigen-antibody complexes, including that for canine parvovirus (CPV) bound with Fabs from several neutralizing MAbs (1, 85–87).

Antibody binding to AAV1 and AAV6. The two different antibodies against AAV1, 4E4 and 5H7 (Table 1), both bound to the protrusions surrounding the 3-fold axis of the capsid but on different surfaces. Fab 4E4 bound to the outer side of the protrusion (i.e., facing away from the 3-fold axis), with the long axis of the Fab pointing toward and across the icosahedral 2-fold axis, while portions of the variable region of the Fab overlap the variable region of a 2-fold-related Fab (Fig. 2A and 3A to D). Consistent with this interpretation, density attributed to the Fab constant and variable chains was approximately 50% of the magnitude (~1.0-σ threshold) of the density observed for the virus capsid and variable region (2.3-σ threshold). Thus, steric hindrance permits only one of two overlapping Fabs to contact the AAV1 capsid at a time (Fig. 3C and D). Residues that comprise the proposed conformational footprint of the fitted 4E4 Fab include 456-AQNK-459 (AAV1 numbering) from one VP monomer and residues 492-TKTDNN N-498 from a 3-fold-related VP monomer (Table 2). These residues correspond to VR-IV and VR-V (Fig. 1), respectively (defined in reference 14). Based on a fitted Web Antibody Modeling (WAM) model of the 4E4 Fab, the PDBePISA application (84) also identified potential interactions at 458-NK-459 on one VP monomer and at 493-KT-494 from the symmetry-related monomer. Although a structure was not determined for 4E4 bound to the AAV6 capsid surface in this study, based on the sequence conservation of these regions to AAV1, it is predicted that the same site would be recognized on the AAV6 capsid surface. Of note,

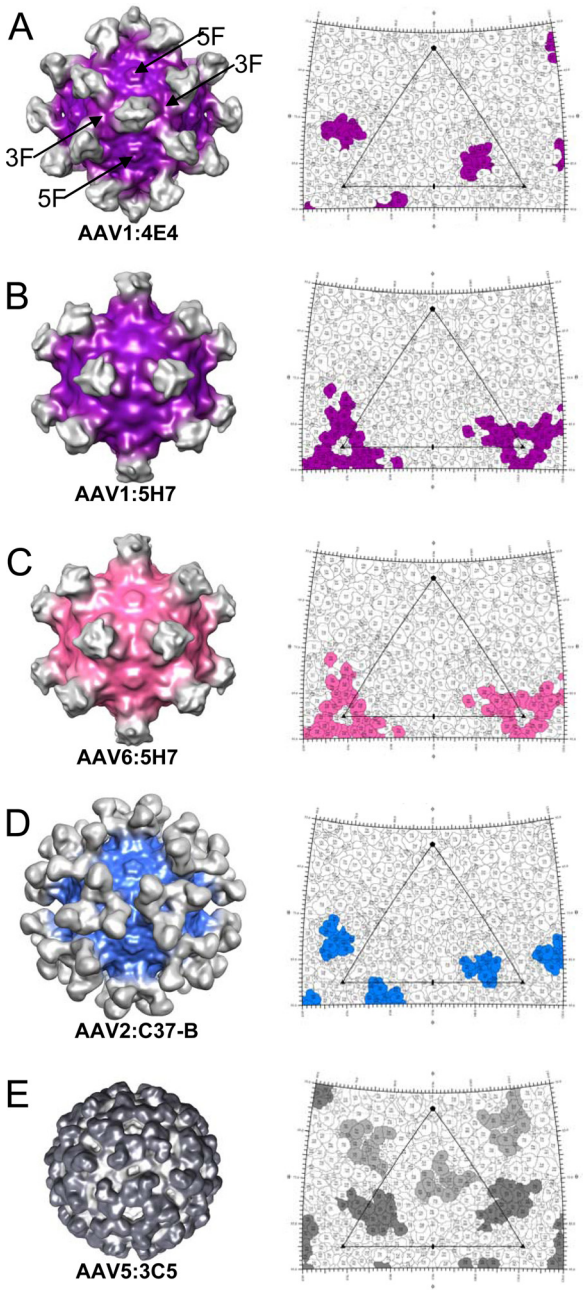

FIG 2 Cryo-EM reconstructions for the AAV:Fab complexes. (A) AAV1:4E4 complex at ~12 Å. (B) AAV1:5H7 complex at ~23 Å. (C) AAV6:5H7 complex at ~15 Å. (D) AAV2:C37B complex at ~11 Å. (E) AAV5:3C5 complex at ~15 Å. The isodensity for each virus-Fab complex is shown (left column) with the antigenic epitopes depicted on a roadmap (103) (right column). Viral surfaces are colored as follows: AAV1, purple; AAV6, pink; AAV2, blue; and AAV5, gray. Fab density is rendered in light grayscale in all cryo-reconstructions except for AAV5, in which the Fab density is dark gray. The arrows on the AAV1:4E4 complex point to approximate locations of the icosahedral symmetry 3- and 5-fold axes indicated by 3F and 5F, respectively. In each roadmap, the Fab footprint is indicated by the capsid color. All density maps are viewed down a 2-fold axis, as indicated by the oval in the accompanying roadmap images. The large open, black triangle on each roadmap depicts a viral asymmetric unit bounded by one 5-fold axis (filled pentagon), two 3-fold axes (filled triangles), and one 2-fold axis (filled oval). In the roadmap of panel E, the dark and light gray footprints represent the contacts between the AAV5 capsid and the constant and variable regions of the 3C5 Fab, respectively.

residue K459 is reported to be important for heparan sulfate proteoglycan (HSPG) recognition by AAV6 (88).

The 5H7 antibody, which cross-reacts with AAV1 and AAV6 (as does 4E4), binds to equivalent regions in the capsids of these two viruses. The 5H7 footprint occurs at the "inward-facing side" of the protrusions surrounding the icosahedral 3-fold axis, and the density was centered at the axis (Fig. 2B and C and 4A). The density in this part of the cryo-reconstruction is consistent with only one Fab, on average, binding to a group of three protrusions. The averaged density for the Fab CDR in contact with the protrusions was observed at a threshold (2.2 σ) similar to that for density in the capsid, whereas the constant regions of the Fabs were observed only at approximately one-third of that density (~0.6 σ). The CDRs in the docked Fab model span two protrusions (Fig. 4B). In this mode of binding, one Fab molecule is bound such that two 3-fold-related sites are sterically blocked, and there is no overlap of the constant regions, which have occupancy of 0.3. The 5H7 footprint mapped to two adjacent AAV1 VP monomers, as observed for the 4E4 binding, but with VR-VIII and VR-V predicted as the sites of interaction (Fig. 4B). Unlike the case in 4E4, two VR-VIIIs from two adjacent VP monomers contribute to the 5H7 epitope. Using the WAM-generated Fab model fitted into the density, the PDBePISA application (84) identified residues 496-NNNS-499 in VR-V and 588-STDPATGD-595 in VR-VIII in one VP (Table 2) as contributing the 5H7 epitope. Capsid residues, 582-VN-583 and H597 near VR-VIII and T494 near VR-V, flank these sites but do not interact directly with the CDRs, based on distance measure cutoffs, and thus may be involved in stabilization of the Fab at the capsid surface.

Antibody binding to AAV2. The C37-B MAb is specific for AAV2 and does not cross-react with other serotypes tested (50). Density for the Fab was observed at the top of each of three protrusions surrounding the 3-fold axis, extending in a radial direction away from the capsid surface; all 60 sites on the capsid were occupied (Fig. 2D). With no sequence available for C37-B, the atomic model of an unrelated Fab (PDB 2FBJ) (77) was docked into the AAV2:C37-B density map to assign the C37-B footprint on AAV2. The binding footprint was located at the top of the protrusions (Fig. 5A) and includes VR-V and VR-VIII (Fig. 5B), as was found for the 5H7 footprint on AAV1 (Table 2). The VR-V contact overlapped the 4E4 footprint on AAV1 (Table 2). However, the 4E4, 5H7, and C37-B Fabs have distinct orientations with respect to the capsid surfaces (compare Fig. 2A and B with D). The C37-B footprint included 492-SADNNNS-498 (AAV2 VP1 numbering) in VR-V from one VP monomer and 585-RGNRQ-589 in VR-VIII from the 3-fold symmetry-related VP (Table 2) by contact analysis in the COOT program (75). Both regions were also identified by the PDBePISA (84) although VR-V was narrowed to the ADNN four-residue stretch by this application. The VR-V residues correlate with previous peptide mapping results where a peptide scanning approach was used to identify two AAV2 stretches (aa 492 to 503 and 601 to 610) as the binding site for C37-B (50). The first of these peptides lies at the surface of the 3-fold protrusion in VR-V, and the second is buried just below the depression at the 3-fold axis. Significantly, residues 492 to 498 lie within the previously mapped epitope and are centrally located within the first peptide sequence, which includes N495 and N496. Mutation of these residues caused a partial reversal of C37-B MAb competition (50). The peptide scanning experiments did not, however, identify the VR-VIII interactions observed in this study.

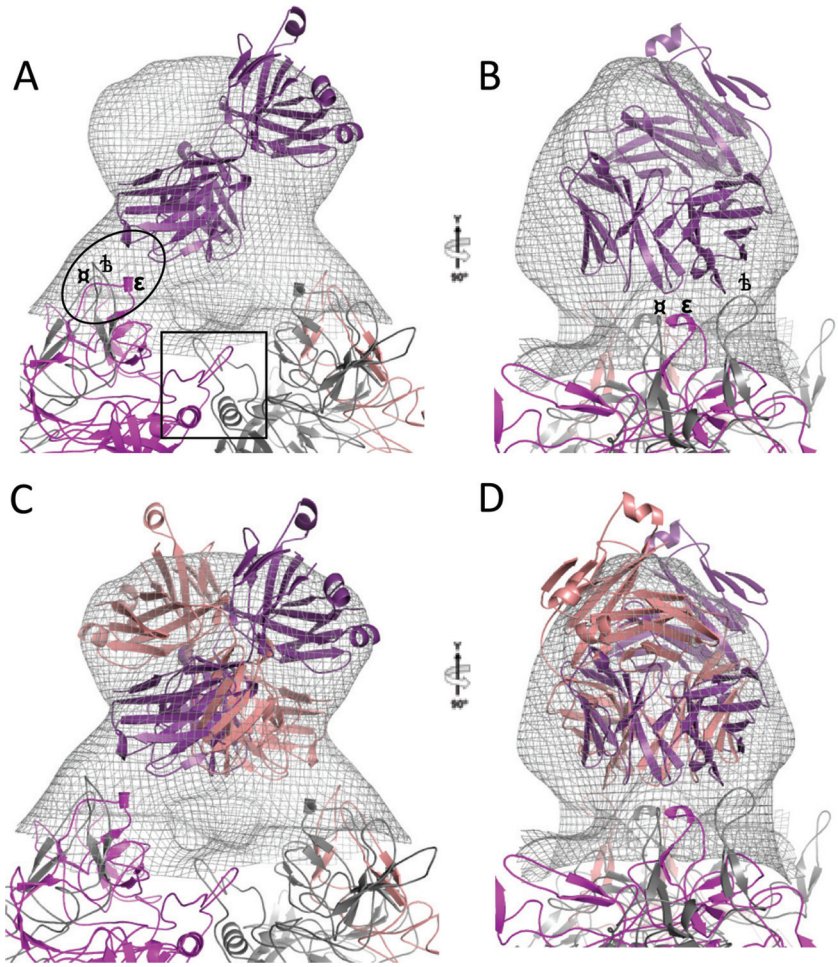

FIG 3 Pseudoatomic model for the AAV1:4E4 Fab complex. (A) A single fitted Fab model (purple ribbon) is shown in the cryo-reconstructed density (gray mesh contoured at 0.5-σ threshold) with the complementarity-determining region (CDR) in close proximity to one 3-fold protrusion (black oval). This view emphasizes the additional density across the 2-fold axis corresponding to the location of the 2-fold-related Fab. The rectangular box delineates the approximate position of the icosahedral 2-fold axis (showing two adjacent helices and protruding VR-IX loops) for the views shown in panels B and D. (B) The figure is the same as that in panel A rotated by 90° about the *y* axis to view the structure from one 3-fold protrusion to another across the 2-fold axes. (C) The figure is the same as that in panel A but with a second Fab model (salmon ribbon) built into the reconstructed density map. This view highlights the overlap between portions of the variable regions of the Fabs bound to each site on the sides of each 3-fold protrusion. (D) The figure is the same as that in panel C rotated 90° about the *y* axis to show the accommodation of the second Fab structure in the reconstructed density map. The approximate location of the VRs for the 3-fold protrusions are labeled in panels A and B as follows: ƀ, VR-IV (gray); ε, VR-V (hot pink); ¤, VR-VIII (gray).

Notably, the region identified within VR-VIII contains two critical arginines, R585 and R588, both of which are important in AAV2 binding to the HSPG receptor (Fig. 5B) (56, 57), and this is consistent with the reported receptor-blocking ability of the C37-B antibody (50).

Antibody binding to AAV5. The 3C5 Fab bound to all 60 sites on the AAV5 capsid but adopted a tangential orientation that obscures a large fraction of the capsid surface, except at the 3-fold axis (Fig. 2E). The density seen in the AAV5:3C5 map thus suggested that both the variable and constant regions of the Fab contact the capsid surface. A difference map generated by subtracting a map of the capsid model from that of the virus-Fab cryo-reconstruction and contoured at a high density threshold (~4.0 σ) aided in the assignment of the potential Fab interaction sites. Two regions of high density were observed: (i) the raised capsid region between the 2-fold and 5-fold depression (2-/5-fold wall) (Fig. 6A, solid box) (site A) and (ii) the region extending from the 2-/5-fold wall toward the 5-fold axis of symmetry (Fig. 6A, dashed box) (site B). Fitting of a Fab model into positive difference density used variable and constant domains that were separated but held in register. During this analysis it was evident that the constant domain of the Fab fitted best into the density designated site A while the wider, variable portion of the Fab structure appeared to fit better into the density at site B. These two sites encompass multiple VRs: site A includes residues 254-SVDGSNAN-261 in VR-I, 374-DN-376 in VR-III, and R483, 485-SVSAFATT-492, R494, E496, and 499-GAS-501 in VR-V; site B includes residues N530 and 532-QPANPGT-538 in VR-VII, 704-DSTGE-708 in VR-IX, and Q246 near S651, 653-VP-54, and 656-SS-657 in the HI loop located between the βH and βI strands (Table 2 and Fig. 6B and C). AAV1 capsids were shown to cross-react with the 3C5 monoclonal antibody (52), and a structural alignment of AAV5 and AAV1 identified both sequence and structural conservation of residues S254, 258-SN-259, and N261 in AAV5 (highlighted in yel-

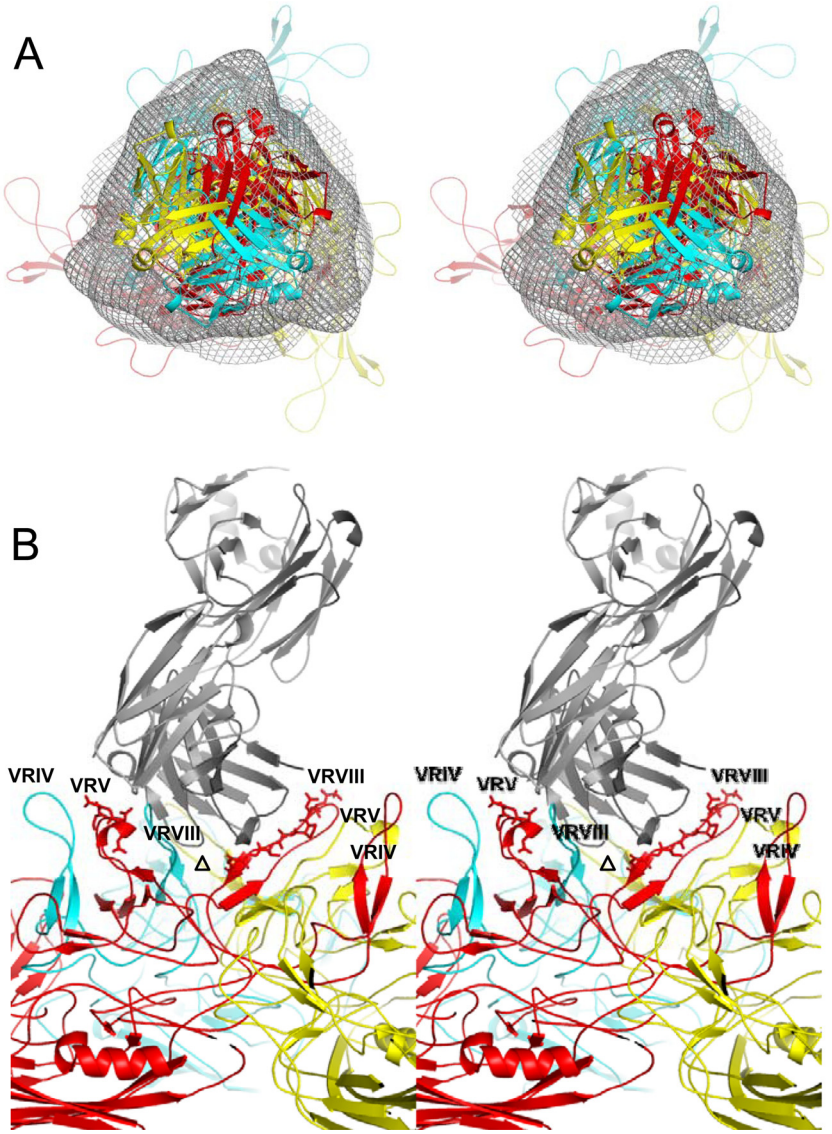

FIG 4 Pseudoatomic model of the AAV1:5H7 Fab complex. (A) Stereo view of three Fab models (red, cyan, and yellow) fitted into density (gray mesh, contoured at a 0.5-σ threshold) protruding from the depression (center) at the icosahedral 3-fold axis. The three VP3 monomers that surround the 3-fold axis are also depicted in red, cyan, and yellow. (B) Enlarged side view of the figure shown in panel A showing a single Fab model (gray). The Fab footprint includes VR-V and VR-VIII (red sticks) of one VP monomer.

low in Fig. 6B and C) with S264, 268-SN-269, and N271 in AAV1 (data not shown) within the footprint. This suggests that the AAV1 interaction may be mediated by the constant region of the Fab. While verification of site B as the CDR binding epitope is required, it is interesting that these residues are located in capsid locations similar to the epitope footprint mapped for the A20 antibody against AAV2 (50, 55, 89). Of all the Fab footprints identified in this study, 3C5 was the least well defined and would benefit from further cryo-EM studies with either the $F(ab')_2$, the intact IgG, or the Fab linked to gold, as well as from mutational analysis of the predicted epitope region for a better understanding of its nonneutralization phenotype.

DISCUSSION

In this study, we have defined the epitope structures on the capsids of AAV1/AAV6 (AAV1/6), AAV2, and AAV5 that are recognized by a set of mouse monoclonal antibodies. The 4E4 and 5H7 antibodies, both of which recognize intact AAV1 and AAV6 capsids, were produced after extended immunization of mice, as was the C37-B IgG against AAV2, and likely represent affinity-mature IgGs. The 3C5 antibody elicited against AAV5 was generated only 4 days after AAV5 capsid immunization of a mouse that had been previously immunized with AAV1. Therefore, 3C5 may represent an affinity-immature antibody (52). Furthermore, it is interesting that the A20 monoclonal, also an IgG3 (50), is reported to interact with similar regions on the AAV2 capsid (55), which is one of the most divergent serotypes from AAV5 (27).

The binding sites for the AAV1/6 and AAV2 antibodies on the different AAV serotypes showed significant overlap with the epitopes mapping close to or on the protrusions that surround the 3-fold axes (Fig. 2A to D). However, the specific sites of interaction varied, with some antibodies binding closer to the top and

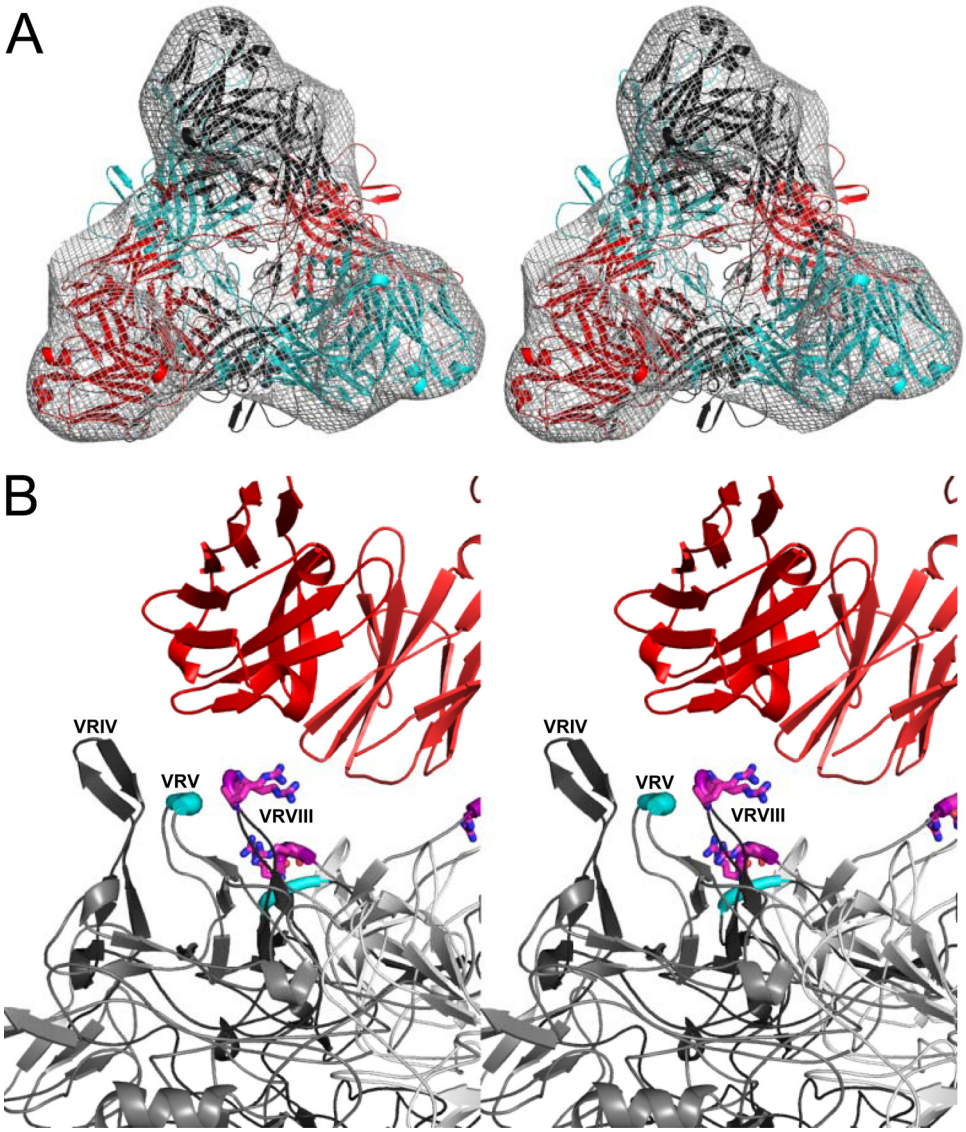

FIG 5 Pseudoatomic model of the AAV2:C37-B Fab complex. (A) Stereo view of a trimer of 3-fold-related VP3 monomers (red, black, and cyan) with a trimer of identically colored Fab models shown within the cryo-reconstructed density (gray mesh contoured at a 0.5-σ threshold). (B) Enlarged side view of the figure shown in panel A of one fitted Fab model (red) that lies above a 3-fold protrusion (in gray ribbon). The epitope consists of VR-V (cyan, 493-ADNNN-496) and VR-VIII (purple, 585-RGNRQ-589). The arginine residues (585 and 588) in VR-VIII that are involved in HSPG binding of AAV2 are rendered as sticks (C terminus in magenta; N terminus in blue). This epitope mapping is consistent with C37-B neutralization of AAV2 steric hindrance of cell surface receptor binding.

others on the side of these morphological features. Although the basis of antigenic variability among different AAV serotypes has yet to be fully defined, the high amino acid sequence variation in the AAV VP loops that form the 3-fold protrusions and the localization of the Fab footprints to these structures indicate that these regions influence AAV serological differences. All footprints occluded adjacent capsid VP subunits, indicating that the virus surfaces form conformational rather than linear epitopes. This is consistent with no reactivity with denatured capsids, as determined by dot blot analyses for the 4E4, 5H7, and 3C5 antibodies (data not shown), and previous reports that the AAV2 C37-B antibody recognizes intact capsids (50). A structural superposition and structure-based sequence alignment of AAV1, AAV2, and AAV6 (Fig. 1B and 7) show that the amino acids of each epitope include variable stretches of sequences that adopt different surface loop conformations (Fig. 1C) (14, 16). Despite this high variability, the epitopes form similar structural features, such as the protrusions surrounding the 3-fold axis or the raised region of the capsid between the 2- and 5-fold axes. Significantly, the ADK8 epitope that mapped onto the AAV8 capsid surface involved VR-VIII (54). Thus, the common AAV VRs appear to confer serotype specificity, suggesting roles in antigenic diversity between the AAVs.

The surfaces of the AAV capsids contacted by the Fabs, including those known to neutralize AAV1 (e.g., 4E4 and 5H7) (52) and AAV2 (e.g., C37-B) (50), did not exhibit any obvious characteristic features other than being at or adjacent to a raised protrusion on the capsid surface. Recognition of these morphological features by antibodies is not surprising since these are the most highly

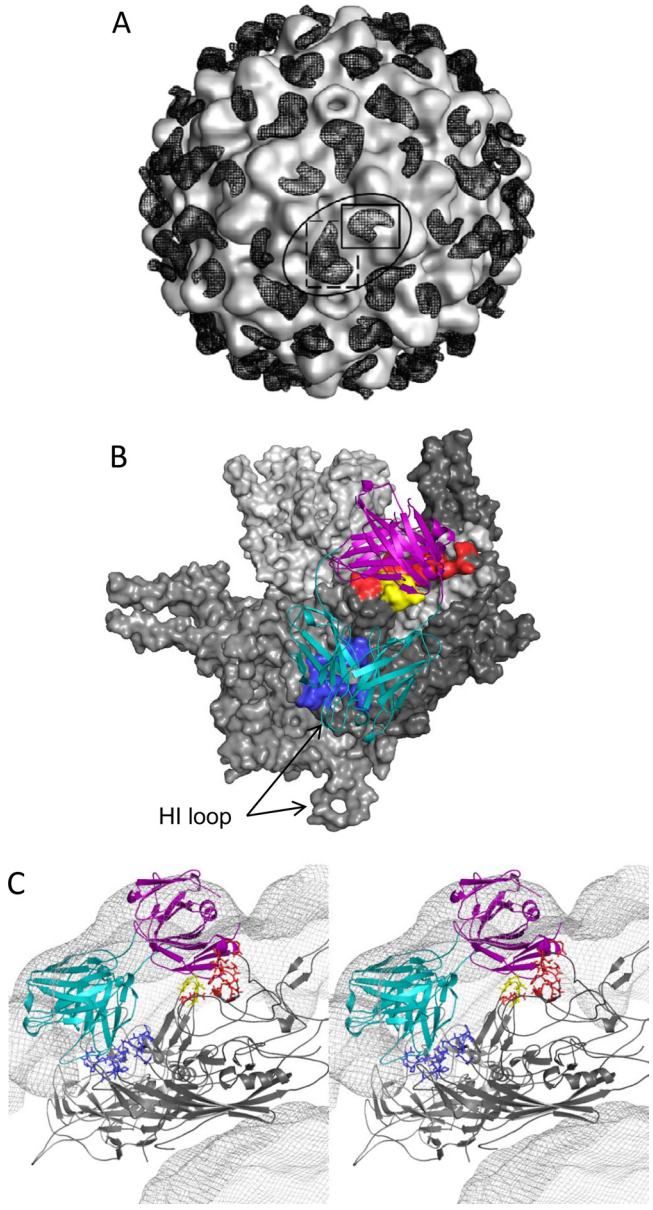

FIG 6 Pseudoatomic model of the AAV5:3C5 complex. (A) Positive difference density (at a threshold of ~4 σ) is shown as the black mesh on the light gray AAV5 capsid model surface. The black oval depicts the region covered by one entire Fab molecule, with the two regions of high-density threshold delineated by solid and dashed boxes. The first region (solid box, site A) is on the 2-/5-fold wall and the second region (dashed box, site B) extends from the 2-/5-fold wall toward the 5-fold axis. (B) Surface representations of three AAV5 VP3 monomers (in shades of gray) highlighting capsid regions involved in contact with the 3C5 Fab. Site A (red) includes four residues common to AAV1 (in yellow), while site B (blue) is shared between two adjacent, 5-fold symmetry-related monomers and includes residues in the HI-loop located on the floor of the 5-fold depression. (C) Stereo image of the Fab density and fitted structures. The two 5-fold-related monomers are shown as gray ribbons, and the proposed epitopes are thickened and colored as mentioned above (site A, red; site B, blue). The yellow region represents identical residues found in the AAV1 capsid. The Fab models were fit into the reconstructed density map at a threshold of 0.5 σ. Variable, cyan; constant, purple.

exposed portions of the capsid surface. This is a common feature for antigenic sites on other parvoviruses, such as AAV8, CPV, and feline panleukopenia virus (FPV), as well as other viral capsids (1, 85–87). However, being raised and/or exposed does not guarantee that a particular feature will serve as an antigenic determinant. For example, the cylinder-shaped surface feature that surrounds each 5-fold axis of symmetry in the AAV capsids did not bind antibodies, and the same features in CPV and FPV capsids also did not bind any of the eight antibodies that have been examined (86). This suggests that structural prominence alone is not sufficient to induce antibody recognition.

The binding orientations observed for most of the Fabs used in this study, coupled with the known flexibility of IgG (90) structures, indicate that most of the MAbs could not bind bivalently to a capsid. Overall, the different AAV footprints are hydrophilic and include a predominance of polar amino acids, but the residue compositions do not differ significantly from those in the remaining portions of the capsid surfaces. Some of the residue types in the epitopes were repeated, with instances of identical three-residue stretches (Table 2 and Fig. 7). The significance, if any, of this observation is unknown.

Numerous studies of other viruses have demonstrated that antibody neutralization can occur by any one of several different mechanisms. These include the following: (i) competition for receptor attachment sites, (ii) abrogation of postentry events during endosomal trafficking, and (iii) stabilization of the capsid against structural changes required for uncoating within the cell (8, 87, 91). Antibodies may block cellular attachment by binding directly to the receptor binding site, or they may block attachment by occluding other regions on the capsid surface when they attach to the capsid in a more tangential orientation. The neutralization mechanisms used by anti-AAV antibodies have yet to be fully investigated although some information is available for some of the antibodies used in this study. The capsids of different AAV serotypes bind a variety of cellular receptors, including glycans such as HSPG, sialic acid, and galactose, and glycoproteins such as α5β1 integrin and platelet-derived growth factor receptor (35, 92–97). For AAV2, the HSPG binding site is close to or overlaps the residues that were identified by peptide mapping to bind the C37-B antibody. C37-B reduces attachment to HSPG (50, 98), which is consistent with the AAV2:C37-B structure (Fig. 2D) where the antibody footprint overlaps the HSPG receptor binding site (Fig. 5B) (56, 57, 99, 100). Monoclonal antibodies 5H7 and 4E4 neutralize cellular infection by AAV1, whereas 3C5 directed against AAV5 had only minor effects at very high antibody concentration (52). The 5H7 and 4E4 antibodies both inhibited cell surface association, suggesting competition with a cell surface receptor, and 4E4 also neutralized virus attachment and entry at high concentrations (52). One of the proposed 5H7 contact peptides, 588-STDPATGD-595, maps structurally close to the positions of two (aa 584 and 598) of the six residues that distinguish the AAV1 and AAV6 capsid VP subunits and, along with residue 531, are reported to influence tissue transduction differences between these two AAV serotypes (16, 58, 101, 102). In addition, one of the proposed 4E4 contact peptides, 456-AQNK-459, includes K459, which is involved in HSPG binding by AAV6 (88). Furthermore, 4E4 binding across the 2-fold axes occludes access to E531/K531 in AAV1/AAV6, respectively, and K531 is known to be involved in HSPG binding by AAV6 (58). These observations support a study that suggests that the neutralization mechanisms

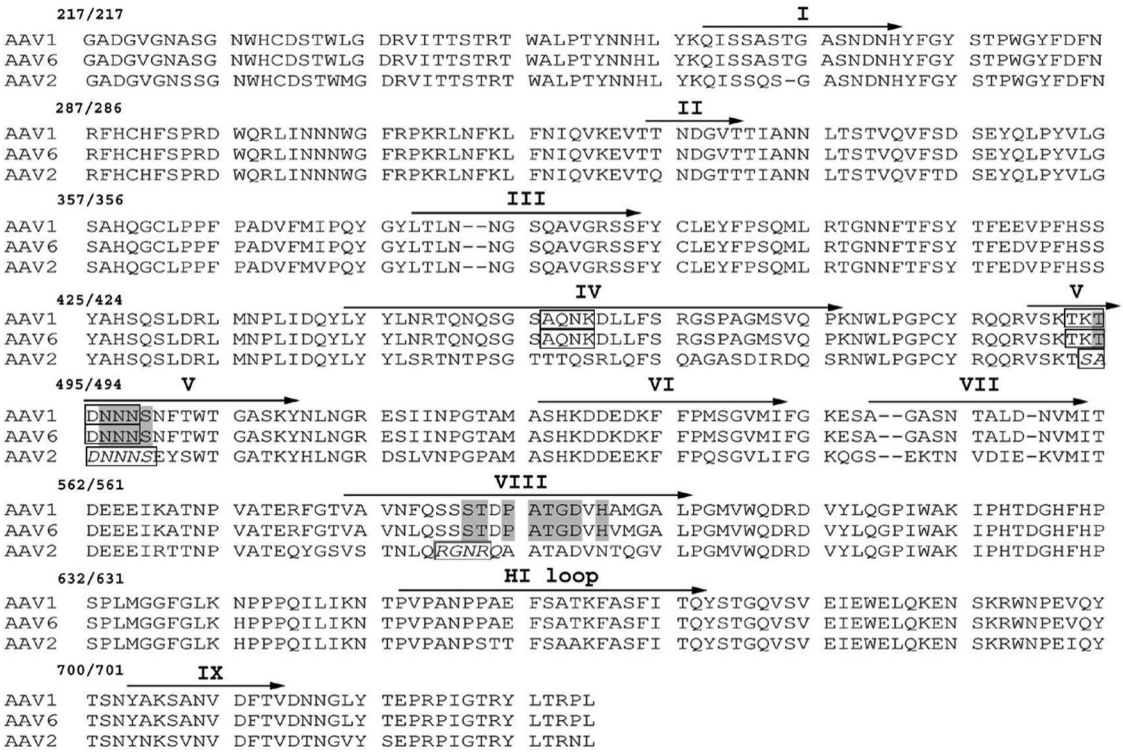

FIG 7 Overlap of proposed AAV epitopes. A structure-based sequence alignment of AAV1, AAV2, and AAV6 with the proposed epitope regions indicated on each corresponding AAV serotype sequence as follows: AAV1:4E4 and AAV6:4E4 sequences are boxed; AAV1:5H7 and AAV6:5H7 sequences are highlighted in light gray; AAV2:C37-B sequences are boxed italics. All epitopes fall into or flank VRs on the capsid surfaces, with overlap among the different Fab complexes. Residue numbers shown above the alignment are in respective order for AAV1/6 and AAV2. Approximate residues contributing to VRs for the serotypes are noted with arrows, and the corresponding VRs are labeled in Roman numerals.

of these two antibodies involve occlusion of the receptor binding sites (52). Also, 4E4 may inhibit a step that occurs after receptor attachment. The lack of robust neutralization of AAV5 by the 3C5 Fab is consistent with that antibody making contact but leaving the 3-fold axes exposed and thus potentially accessible to receptors. Furthermore, residue A581 is proposed to play a role in sialic acid recognition and airway cellular transduction in AAV5 (59) but is not part of the Fab binding footprint, which is consistent with lack of virus neutralization by the antibody.

Here, we have shown that several mouse monoclonal antibodies raised against AAV capsids recognize a relatively small portion of the protrusions that surround each 3-fold axis, but there is variability in the mode and stoichiometry of binding. If human antibodies bind similarly to small regions of the AAV capsids, it should be possible to engineer mutations in AAV capsids that block a variety of antibody interactions, e.g., by introduction of insertion peptides at the mapped sites or by introduction of nonconserved and nonrepeated amino acid sequences. It would also be of interest to determine if different isotypes or subclasses of antibodies prefer certain regions or structures on the capsid surface. Such changes could preclude the binding of most antibodies while retaining functions needed to deliver genetic payloads to target tissues.

ACKNOWLEDGMENTS

We thank Sujata Halder, Department of Biochemistry and Molecular Biology, University of Florida, for her assistance in the preparation of Fig. 2.

This project was funded in part by NIH grants R21AI072341 (to C.R.P. and M.A.-M.), R01 AI072176-01 (to M.A.-M. and R.J.S.), R01 GM082946 (to M.A.-M., R.M., N.M., and S.Z.), P01 HL112761 (to R.J.S), R37 GM-33050 (to T.S.B.), and 1S10 RR020016 (to T.S.B.), by NIH Intramural funds (to J.A.C.), and by support from the University of California—San Diego (UCSD) and the Agouron Foundation (to T.S.B.) to establish cryo-EM facilities at UCSD.

REFERENCES

1. **Moskalenko M, Chen L, van Roey M, Donahue BA, Snyder RO, McArthur JG, Patel SD.** 2000. Epitope mapping of human anti-adeno-associated virus type 2 neutralizing antibodies: implications for gene therapy and virus structure. J. Virol. **74:**1761–1766.
2. **Manno CS, Pierce GF, Arruda VR, Glader B, Ragni M, Rasko JJ, Rasko J, Ozelo MC, Hoots K, Blatt P, Konkle B, Dake M, Kaye R, Razavi M, Zajko A, Zehnder J, Rustagi PK, Nakai H, Chew A, Leonard D, Wright JF, Lessard RR, Sommer JM, Tigges M, Sabatino D, Luk A, Jiang H, Mingozzi F, Couto L, Ertl HC, High KA, Kay MA.** 2006. Successful transduction of liver in hemophilia by AAV-factor IX and limitations imposed by the host immune response. Nat. Med. **12:**342–347.
3. **Zaiss AK, Muruve DA.** 2008. Immunity to adeno-associated virus vectors in animals and humans: a continued challenge. Gene Ther. **15:**808–816.
4. **Wang L, Calcedo R, Bell P, Lin J, Grant RL, Siegel DL, Wilson JM.** 2011. Liver gene transfer with vectors based on adeno-associated virus 8 in non-human primates: impact of pre-existing immunity. Hum. Gene Ther. **22:**1389–1401.
5. **Bachmann MF, Zinkernagel RM.** 1996. The influence of virus structure on antibody responses and virus serotype formation. Immunol. Today **17:**553–558.
6. **Dorner T, Radbruch A.** 2007. Antibodies and B cell memory in viral immunity. Immunity **27:**384–392.
7. **Hangartner L, Zinkernagel RM, Hengartner H.** 2006. Antiviral anti-

body responses: the two extremes of a wide spectrum. Nature Rev. Immunol. **6:**231–243.
8. **Reading SA, Dimmock NJ.** 2007. Neutralization of animal virus infectivity by antibody. Arch. Virol. **152:**1047–1059.
9. **Grieger JC, Snowdy S, Samulski RJ.** 2006. Separate basic region motifs within the adeno-associated virus capsid proteins are essential for infectivity and assembly. J. Virol. **80:**5199–5210.
10. **Sonntag F, Bleker S, Leuchs B, Fischer R, Kleinschmidt JA.** 2006. Adeno-associated virus type 2 capsids with externalized VP1/VP2 trafficking domains are generated prior to passage through the cytoplasm and are maintained until uncoating occurs in the nucleus. J. Virol. **80:**11040–11054.
11. **Stahnke S, Lux K, Uhrig S, Kreppel F, Hosel M, Coutelle O, Ogris M, Hallek M, Buning H.** 2011. Intrinsic phospholipase A2 activity of adeno-associated virus is involved in endosomal escape of incoming particles. Virology **409:**77–83.
12. **Girod A, Ried M, Wobus C, Lahm H, Leike K, Kleinschmidt J, Deléage G, Hallek M.** 1999. Genetic capsid modifications allow efficient retargeting of adeno-associated virus type 2. Nat. Med. **5:**1052–1056.
13. **Xie Q, Bu W, Bhatia S, Hare J, Somasundaram T, Azzi A, Chapman MS.** 2002. The atomic structure of adeno-associated virus (AAV-2), a vector for human gene therapy. Proc. Natl. Acad. Sci. U. S. A. **99:**10405–10410.
14. **Govindasamy L, Padron E, McKenna R, Muzyczka N, Kaludov N, Chiorini JA, Agbandje-McKenna M.** 2006. Structurally mapping the diverse phenotype of adeno-associated virus serotype 4. J. Virol. **80:**11556–11570.
15. **Nam H-J, Lane MD, Padron E, Gurda B, McKenna R, Kohlbrenner E, Aslanidi G, Byrne B, Muzyczka N, Zolotukhin S, Agbandje-McKenna M.** 2007. Structure of adeno-associated virus serotype 8, a gene therapy vector. J. Virol. **81:**12260–12271.
16. **Ng R, Govindasamy L, Gurda BL, McKenna R, Kozyreva OG, Samulski RJ, Parent KN, Baker TS, Agbandje-McKenna M.** 2010. Structural characterization of the dual glycan binding adeno-associated virus serotype 6. J. Virol. **84:**12945–12957.
17. **Lerch TF, Xie Q, Chapman MS.** 2010. The structure of adeno-associated virus serotype 3B (AAV-3B): insights into receptor binding and immune evasion. Virology **403:**26–36.
18. **Chapman MS, Agbandje-McKenna M.** 2006. Atomic structures of viral particles, p 107–123. *In* Kerr JR, Cotmore SF, Bloom ME, Linden RL, Parrish CR (ed), Parvoviruses. Edward Arnold, Ltd., New York, NY.
19. **Agbandje-McKenna M, Chapman MS.** 2006. Correleating structure with function in the viral capsid, p 125–139. *In* Kerr JR, Cotmore SF, Bloom ME, Linden RM, Parrish CR (ed), Parvoviruses. Edward Arnold, Ltd., New York, NY.
20. **Agbandje-McKenna M, Kleinschmidt J.** 2011. AAV capsid structure and cell interactions. Methods Mol. Biol. **807:**47–92.
21. **Atchison RW, Casto BC, Hammon WM.** 1965. Adenovirus-associated defective virus particles. Science **149:**754–756.
22. **Hoggan MD, Blacklow NR, Rowe WP.** 1966. Studies of small DNA viruses found in various adenovirus preparations: physical, biological, and immunological characteristics. Proc. Natl. Acad. Sci. U. S. A. **55:**1467–1474.
23. **Parks WP, Green M, Pina M, Melnick JL.** 1967. Physicochemical characterization of adeno-associated satellite virus type 4 and its nucleic acid. J. Virol. **1:**980–987.
24. **Bantel-Schaal U, zur Hausen H.** 1984. Characterization of the DNA of a defective human parvovirus isolated from a genital site. Virology **134:**52–63.
25. **Rutledge EA, Halbert CL, Russell DW.** 1998. Infectious clones and vectors derived from adeno-associated virus (AAV) serotypes other than AAV type 2. J. Virol. **72:**309–319.
26. **Gao G-P, Alvira MR, Wang L, Calcedo R, Johnston J, Wilson JM.** 2002. Novel adeno-associated viruses from rhesus monkeys as vectors for human gene therapy. Proc. Natl. Acad. Sci. U. S. A. **99:**11854–11859.
27. **Gao G, Vandenberghe LH, Alvira MR, Lu Y, Calcedo R, Zhou X, Wilson JM.** 2004. Clades of adeno-associated viruses are widely disseminated in human tissues. J. Virol. **78:**6381–6388.
28. **Mori S, Wang L, Takeuchi T, Kanda T.** 2004. Two novel adeno-associated viruses from cynomolgus monkey: pseudotyping characterization of capsid protein. Virology **330:**375–383.
29. **Schmidt M, Voutetakis A, Afione S, Zheng C, Mandikian D, Chiorini JA.** 2008. Adeno-associated virus type 12 (AAV12): a novel AAV serotype with sialic acid- and heparan sulfate proteoglycan-independent transduction activity. J. Virol. **82:**1399–1406.
30. **Dutta SK.** 1975. Isolation and characterization of an adenovirus and isolation of its adenovirus-associated virus in cell culture from foals with respiratory tract disease. Am. J. Vet. Res. **36:**247–250.
31. **Farkas SL, Zadori Z, Benko M, Essbauer S, Harrach B, Tijssen P.** 2004. A parvovirus isolated from royal python (*Python regius*) is a member of the genus *Dependovirus*. J. Gen. Virol. **85:**555–561.
32. **Bossis I, Chiorini JA.** 2003. Cloning of an avian adeno-associated virus (AAAV) and generation of recombinant AAAV particles. J. Virol. **77:**6799–6810.
33. **Arbetman AE, Lochrie M, Zhou S, Wellman J, Scallan C, Doroudchi MM, Randlev B, Patarroyo-White S, Liu T, Smith P, Lehmkuhl H, Hobbs LA, Pierce GF, Colosi P.** 2005. Novel caprine adeno-associated virus (AAV) capsid (AAV-Go.1) is closely related to the primate AAV-5 and has unique tropism and neutralization properties. J. Virol. **79:**15238–15245.
34. **Schmidt M, Grot E, Cervenka P, Wainer S, Buck C, Chiorini JA.** 2006. Identification and characterization of novel adeno-associated virus isolates in ATCC virus stocks. J. Virol. **80:**5082–5085.
35. **Wu Z, Miller E, Agbandje-McKenna M, Samulski RJ.** 2006. α2,3 and α2,6 N-linked sialic acids facilitate efficient binding and transduction by adeno-associated virus types 1 and 6. J. Virol. **80:**9093–9103.
36. **Schmidt M, Govindasamy L, Afione S, Kaludov N, Agbandje-McKenna M, Chiorini JA.** 2008. Molecular characterization of the heparin-dependent transduction domain on the capsid of a novel adeno-associated virus isolate, AAV(VR-942). J. Virol. **82:**8911–8916.
37. **Zincarelli C, Soltys S, Rengo G, Rabinowitz JE.** 2008. Analysis of AAV serotypes 1–9 mediated gene expression and tropism in mice after systemic injection. Mol. Ther. **16:**1073–1080.
38. **Mueller C, Flotte TR.** 2008. Clinical gene therapy using recombinant adeno-associated virus vectors. Gene Ther. **15:**858–863.
39. **Calcedo R, Vandenberghe LH, Gao G, Lin J, Wilson JM.** 2009. Worldwide epidemiology of neutralizing antibodies to adeno-associated viruses. J. Infect. Dis. **199:**381–390.
40. **Halbert CL, Miller AD, McNamara S, Emerson J, Gibson RL, Ramsey B, Aitken ML.** 2006. Prevalence of neutralizing antibodies against adeno-associated virus (AAV) types 2, 5, and 6 in cystic fibrosis and normal populations: Implications for gene therapy using AAV vectors. Hum. Gene Ther. **17:**440–447.
41. **Vandenberghe LH, Wilson JM.** 2007. AAV as an immunogen. Curr. Gene Ther. **7:**325–333.
42. **Bessis N, GarciaCozar FJ, Boissier MC.** 2004. Immune responses to gene therapy vectors: influence on vector function and effector mechanisms. Gene Ther. **11**(Suppl 1):S10–S17.
43. **Mingozzi F, High KA.** 2007. Immune responses to AAV in clinical trials. Curr. Gene Ther. **7:**316–324.
44. **Cottard V, Valvason C, Falgarone G, Lutomski D, Boissier Bessis M-CN.** 2004. Immune response against gene therapy vectors: influence of synovial fluid on adeno-associated virus mediated gene transfer to chondrocytes. J. Clin. Immunol. **24:**162–169.
45. **Li H, Lin SW, Giles-Davis W, Li Y, Zhou D, Xiang ZQ, High KA, Ertl HCJ.** 2009. A preclinical animal model to assess the effect of pre-existing immunity on AAV-mediated gene transfer. Mol. Ther. **17:**1215–1224.
46. **Xiao W, Chirmule N, Schnell MA, Tazelaar J, Hughes JV, Wilson JM.** 2000. Route of administration determines induction of T-cell-independent humoral responses to adeno-associated virus vectors. Mol. Ther. **1:**323–329.
47. **Zaldumbide A, Hoeben RC.** 2008. How not to be seen: immune-evasion strategies in gene therapy. Gene Ther. **15:**239–246.
48. **Dobrzynski E, Fitzgerald JC, Cao O, Mingozzi F, Wang L, Herzog RW.** 2006. Prevention of cytotoxic T lymphocyte responses to factor IX-expressing hepatocytes by gene transfer-induced regulatory T cells. Proc. Natl. Acad. Sci. U. S. A. **103:**4592–4597.
49. **Peden CS, Burger C, Muzyczka N, Mandel RJ.** 2004. Circulating anti-wild-type adeno-associated virus type 2 (AAV2) antibodies inhibit recombinant AAV2 (rAAV2)-mediated, but not rAAV5-mediated, gene transfer in the brain. J. Virol. **78:**6344–6359.
50. **Wobus CE, Hügle-Dörr B, Girod A, Petersen G, Hallek M, Kleinschmidt JA.** 2000. Monoclonal antibodies against the adeno-associated virus type 2 (AAV-2) capsid: epitope mapping and identification of capsid domains involved in AAV-2-cell interaction and neutralization of AAV-2 infection. J. Virol. **74:**9281–9293.

51. **Kuck D, Kern A, Kleinschmidt JA.** 2007. Development of AAV serotype-specific ELISAs using novel monoclonal antibodies. J. Virol. Methods **140:**17–24.
52. **Harbison CE, Weichert WS, Gurda BL, Chiorini JA, Agbandje-McKenna M, Parrish CR.** 2011. Examining the cross-reactivity and neutralization mechanisms of a panel of monoclonal antibodies against adeno-associated virus serotypes 1 and 5. J. Gen. Virol. **93:**347–355.
53. **Huttner NA, Girod A, Perabo L, Edbauer D, Kleinschmidt JA, Buning H, Hallek M.** 2003. Genetic modifications of the adeno-associated virus type 2 capsid reduce the affinity and the neutralizing effects of human serum antibodies. Gene Ther. **10:**2139–2147.
54. **Gurda BL, Raupp C, Popa-Wagner R, Naumer M, Olson NH, Ng R, McKenna R, Baker TS, Kleinschmidt JA, Agbandje-McKenna M.** 2012. Mapping a neutralizing epitope onto the capsid of adeno-associated virus serotype 8. J. Virol. **86:**7739–7751.
55. **McCraw DM, O'Donnell JK, Taylor KA, Stagg SM, Chapman MS.** 2012. Structure of adeno-associated virus-2 in complex with neutralizing monoclonal antibody A20. Virology **431:**40–49.
56. **Kern A, Schmidt K, Leder C, Müller OJ, Wobus CE, Bettinger K, Von der Lieth CW, King JA, Kleinschmidt JA.** 2003. Identification of a heparin-binding motif on adeno-associated virus type 2 capsids. J. Virol. **77:**11072–11081.
57. **Opie SR, Warrington KH, Agbandje-McKenna M, Zolotukhin S, Muzyczka N.** 2003. Identification of amino acid residues in the capsid proteins of adeno-associated virus type 2 that contribute to heparan sulfate proteoglycan binding. J. Virol. **77:**6995–7006.
58. **Wu Z, Asokan A, Grieger JC, Govindasamy L, Agbandje-McKenna M, Samulski RJ.** 2006. Single amino acid changes can influence titer, heparin binding, and tissue tropism in different adeno-associated virus serotypes. J. Virol. **80:**11393–11397.
59. **Excoffon KJDA, Koerber JT, Dickey DD, Murtha M, Keshavjee S, Kaspar BK, Zabner J, Schaffer DV.** 2009. Directed evolution of adeno-associated virus to an infectious respiratory virus. Proc. Natl. Acad. Sci. U. S. A. **106:**3865–3870.
60. **DiMattia M, Govindasamy L, Levy HC, Gurda-Whitaker B, Kalina A, Kohlbrenner E, Chiorini JA, McKenna R, Muzyczka N, Zolotukhin S, Agbandje-McKenna M.** 2005. Production, purification, crystallization and preliminary X-ray structural studies of adeno-associated virus serotype 5. Acta Crystallogr. Sect. F Struct. Biol. Cryst. Commun. **61:**917–921.
61. **Miller EB, Gurda-Whitaker B, Govindasamy L, McKenna R, Zolotukhin S, Muzyczka N, Agbandje-McKenna M.** 2006. Production, purification and preliminary X-ray crystallographic studies of adeno-associated virus serotype 1. Acta Crystallogr. Sect. F Struct. Biol. Cryst. Commun. **62:**1271–1274.
62. **Zolotukhin S, Potter M, Zolotukhin I, Sakai Y, Loiler S, Fraites TJ, Chiodo VA, Phillipsberg T, Muzyczka N, Hauswirth WW, Flotte TR, Byrne BJ, Snyder RO.** 2002. Production and purification of serotype 1, 2, and 5 recombinant adeno-associated viral vectors. Methods **28:**158–167.
63. **Martin AC, Cheetham JC, Rees AR.** 1989. Modeling antibody hypervariable loops: a combined algorithm. Proc. Natl. Acad. Sci. U. S. A. **86:**9268–9272.
64. **Adrian M, Dubochet J, Lepault J, McDowall AW.** 1984. Cryo-electron microscopy of viruses. Nature **308:**32–36.
65. **Dubochet J, Adrian M, Chang JJ, Homo JC, Lepault J, McDowall AW, Schultz P.** 1988. Cryo-electron microscopy of vitrified specimens. Q. Rev. Biophys. **21:**129–228.
66. **Baker TS, Olson NH, Fuller SD.** 1999. Adding the third dimension to virus life cycles: three-dimensional reconstruction of icosahedral viruses from cryo-electron micrographs. Microbiol. Mol. Biol. Rev. **63:**862–922.
67. **Yan X, Sinkovits RS, Baker TS.** 2007. AUTO3DEM—an automated and high throughput program for image reconstruction of icosahedral particles. J. Struct. Biol. **157:**73–82.
68. **Gurda BL, Parent KN, Bladek H, Sinkovits RS, DiMattia MA, Rence C, Castro A, McKenna R, Olson N, Brown K, Baker TS, Agbandje-McKenna M.** 2010. Human bocavirus capsid structure: insights into the structural repertoire of the *Parvoviridae*. J. Virol. **84:**5880–5889.
69. **Yan X, Dryden KA, Tang J, Baker TS.** 2007. Ab initio random model method facilitates 3D reconstruction of icosahedral particles. J. Struct. Biol. **157:**211–225.
70. **Bowman VD, Chase ES, Franz AWE, Chipman PR, Zhang X, Perry KL, Baker TS, Smith TJ.** 2002. An antibody to the putative aphid recognition site on cucumber mosaic virus recognizes pentons but not hexons. J. Virol. **76:**12250–12258.
71. **Zhang X, Walker SB, Chipman PR, Nibert ML, Baker TS.** 2003. Reovirus polymerase lambda 3 localized by cryo-electron microscopy of virions at a resolution of 7.6 Å. Nat. Struct. Biol. **10:**1011–1018.
72. **van Heel M, Schatz M.** 2005. Fourier shell correlation threshold criteria. J. Struct. Biol. **151:**250–262.
73. **Pettersen EF, Goddard TD, Huang CC, Couch GS, Greenblatt DM, Meng EC, Ferrin TE.** 2004. UCSF Chimera—a visualization system for exploratory research and analysis. J. Comput. Chem. **25:**1605–1612.
74. **Chacon P, Wriggers W.** 2002. Multi-resolution contour-based fitting of macromolecular structures. J. Mol. Biol. **317:**375–384.
75. **Emsley P, Cowtan K.** 2004. COOT: model-building tools for molecular graphics. Acta Crystallogr. D Biol. Crystallogr. **60:**2126–2132.
76. **Kleywegt GJ, Jones TA.** 1996. xdlMAPMAN and xdlDATAMAN—programs for reformatting, analysis and manipulation of biomacromolecular electron-density maps and reflection data sets. Acta Crystallogr. D Biol. Crystallogr. **52:**826–828.
77. **Suh SW, Bhat TN, Navia MA, Cohen GH, Rao DN, Rudikoff S, Davies DR.** 1986. The galactan-binding immunoglobulin Fab J539: an X-ray diffraction study at 2.6-Å resolution. Proteins **1:**74–80.
78. **Strong RK, Campbell R, Rose DR, Petsko GA, Sharon J, Margolies MN.** 1991. Three-dimensional structure of murine anti-*p*-azophenylarsonate Fab 36–71. 1. X-ray crystallography, site-directed mutagenesis, and modeling of the complex with hapten. Biochemistry **30:**3739–3748.
79. **Guddat LW, Shan L, Broomell C, Ramsland PA, Fan Z, Anchin JM, Linthicum DS, Edmundson AB.** 2000. The three-dimensional structure of a complex of a murine Fab (NC10.14) with a potent sweetener (NC174): an illustration of structural diversity in antigen recognition by immunoglobulins. J. Mol. Biol. **302:**853–872.
80. **Goddard TD, Huang CC, Ferrin TE.** 2007. Visualizing density maps with UCSF Chimera. J. Struct. Biol. **157:**281–287.
81. **Heymann JB, Belnap DM.** 2007. Bsoft: image processing and molecular modeling for electron microscopy. J. Struct. Biol. **157:**3–18.
82. **Emsley P, Lohkamp B, Scott WG, Cowtan K.** 2010. Features and development of Coot. Acta Crystallogr. D Biol. Crystallogr. **66:**486–501.
83. **Brooks CL, Blackler RJ, Sixta G, Kosma P, Muller-Loennies S, Brade L, Hirama T, MacKenzie CR, Brade H, Evans SV.** 2010. The role of CDR H3 in antibody recognition of a synthetic analog of a lipopolysaccharide antigen. Glycobiology **20:**138–147.
84. **Krissinel E, Henrick K.** 2007. Inference of macromolecular assemblies from crystalline state. J. Mol. Biol. **372:**774–797.
85. **Kaufmann B, López-Bueno A, Mateu MG, Chipman PR, Nelson CDS, Parrish CR, Almendral JM, Rossmann MG.** 2007. Minute virus of mice, a parvovirus, in complex with the Fab fragment of a neutralizing monoclonal antibody. J. Virol. **81:**9851–9858.
86. **Hafenstein S, Bowman VD, Sun T, Nelson CDS, Palermo LM, Chipman PR, Battisti AJ, Parrish CR, Rossmann MG.** 2009. Structural Comparison of Different Antibodies Interacting with Parvovirus Capsids. J. Virol. **83:**5556–5566.
87. **Smith TJ.** 2003. Structural studies on antibody-virus complexes. Adv. Protein Chem. **64:**409–453.
88. **Xie Q, Lerch TF, Meyer NL, Chapman MS.** 2011. Structure-function analysis of receptor-binding in adeno-associated virus serotype 6 (AAV-6). Virology **420:**10–19.
89. **Lochrie MA, Tatsuno GP, Christie B, McDonnell JW, Zhou S, Surosky R, Pierce GF, Colosi P.** 2006. Mutations on the external surfaces of adeno-associated virus type 2 capsids that affect transduction and neutralization. J. Virol. **80:**821–834.
90. **Stanfield RL, Zemla A, Wilson IA, Rupp B.** 2006. Antibody elbow angles are influenced by their light chain class. J. Mol. Biol. **357:**1566–1574.
91. **Law M, Hangartner L.** 2008. Antibodies against viruses: passive and active immunization. Curr. Opin. Immunol. **20:**486–492.
92. **Summerford C, Samulski RJ.** 1998. Membrane-associated heparan sulfate proteoglycan is a receptor for adeno-associated virus type 2 virions. J. Virol. **72:**1438–1445.
93. **Asokan A, Hamra JB, Govindasamy L, Agbandje-McKenna M, Samulski RJ.** 2006. Adeno-associated virus type 2 contains an integrin α5β1 binding domain essential for viral cell entry. J. Virol. **80:**8961–8969.
94. **Kaludov N, Brown KE, Walters RW, Zabner J, Chiorini JA.** 2001. Adeno-associated virus serotype 4 (AAV4) and AAV5 both require sialic

acid binding for hemagglutination and efficient transduction but differ in sialic acid linkage specificity. J. Virol. **75:**6884–6893.
95. **Walters RW, Yi SM, Keshavjee S, Brown KE, Welsh MJ, Chiorini JA, Zabner J.** 2001. Binding of adeno-associated virus type 5 to 2,3-linked sialic acid is required for gene transfer. J. Biol. Chem. **276:**20610–20616.
96. **Shen S, Bryant KD, Brown SM, Randell SH, Asokan A.** 2011. Terminal N-linked galactose is the primary receptor for adeno-associated virus 9. J. Biol. Chem. **286:**13532–13540.
97. **Di Pasquale G, Davidson BL, Stein CS, Martins I, Scudiero D, Monks A, Chiorini JA.** 2003. Identification of PDGFR as a receptor for AAV-5 transduction. Nat. Med. **9:**1306–1312.
98. **Wistuba A, Kern A, Weger S, Grimm D, Kleinschmidt JA.** 1997. Subcellular compartmentalization of adeno-associated virus type 2 assembly. J. Virol. **71:**1341–1352.
99. **Levy HC, Bowman VD, Govindasamy L, McKenna R, Nash K, Warrington K, Chen W, Muzyczka N, Yan X, Baker TS, Agbandje-McKenna M.** 2009. Heparin binding induces conformational changes in adeno-associated virus serotype 2. J. Struct. Biol. **165:**146–156.
100. **O'Donnell J, Taylor KA, Chapman MS.** 2009. Adeno-associated virus-2 and its primary cellular receptor: cryo-EM structure of a heparin complex. Virology **385:**434–443.
101. **Li W, Zhang L, Johnson JS, Zhijian W, Grieger JC, Ping-Jie X, Drouin LM, Agbandje-McKenna M, Pickles RJ, Samulski RJ.** 2009. Generation of novel AAV variants by directed evolution for improved CFTR delivery to human ciliated airway epithelium. Mol. Ther. **17:**2067–2077.
102. **Limberis MP, Vandenberghe LH, Zhang L, Pickles RJ, Wilson JM.** 2009. Transduction efficiencies of novel AAV vectors in mouse airway epithelium in vivo and human ciliated airway epithelium in vitro. Mol. Ther. **17:**294–301.
103. **Xiao C, Rossmann MG.** 2007. Interpretation of electron density with stereographic roadmap projections. J. Struct. Biol. **158:**182–187.